Mixing in a vortex breakdown flow

Patrice Meunier, Kerry Hourigan

▶ To cite this version:

HAL Id: hal-00947588

https://hal.archives-ouvertes.fr/hal-00947588

Submitted on 19 Feb 2014

Mixing in a vortex breakdown flow

P. MEUNIER[1,2] **and K. HOURIGAN**[2,3]

[1]IRPHE UMR7342, CNRS, Aix Marseille Université, Centrale Marseille
13013, Marseille, France
[2] Division of Biological Engineering, Monash University, Melbourne, Victoria 3800 Australia
[3] Department of Mechanical and Aerospace Engineering, Monash University, Melbourne,
Victoria 3800 Australia

This paper presents experimental and theoretical results on the mixing inside a cylinder with a rotating lid. The helical flow that is created by the rotation of the disk is well known to exhibit a vortex breakdown bubble over a finite range of Reynolds numbers. The mixing properties of the flow are analyzed quantitatively by measuring the exponential decay of the variance as a function of time. This homogenization time is extremely sensitive to the asymmetries of the flow, which are introduced by tilting the rotating or the stationary disk and accurately measured by Particle Image Velocimetry (PIV).

In the absence of vortex breakdown, the homogenization time is strongly decreased (by a factor 10) with only a moderate tilt angle of the rotating lid (of the order of 15 degrees). This phenomenon can be explained by the presence of small radial jets at the periphery which create a strong convective mixing. A simple model of exchange flow between the periphery and the bulk correctly predicts the scaling laws for the homogenization time.

In the presence of vortex breakdown, the scalar is trapped inside the vortex breakdown bubble, and thus increases substantially the time needed for homogenization. Curiously, the tilt of the rotating lid has a weak effect on the mixing, but a small tilt of the stationary disk (of the order of 2 degrees) strongly decreases (by a factor 10) the homogenization time. Even more surprising is that the homogenization time diverges when the size of the bubble vanishes. All these features are recovered by applying the Melnikov theory to calculate the volume of the lobes that exit the bubble. It is the first time that this technique has been applied to a 3D stationary flow with a non-axisymmetric perturbation and compared with experimental results, although it has been applied often to 2D flows with a periodic perturbation.

---

1. Introduction

It is well known that helical flows are unstable with respect to vortex breakdown, leading to a complex geometry of the streamlines with a barrier to transport between the inner part and the outer part of the bubble. The goal of this paper is to quantify experimentally the mixing in this 3D flow and to compare it with available theories derived for chaotic advection.

Vortex breakdown usually refers to a recirculating bubble that occurs past a stagnation point due to the rapid expansion of a thin vortex into a much broader one (Leibovich 1978). It is a surprising and practically important phenomenon, which has been observed in many different swirling flows from geophysical to industrial applications. Vortex breakdown was first observed over the delta wings of aircrafts (Wentz & Kohlman 1971; Hall 1972; Lowson & Riley 1995) where it creates a sudden drop of the lift and an increase

in the drag, possibly leading to a loss of aircraft control (Escudier 1988). By contrast, it is beneficial in the geophysical context since it decreases the maximal velocities of tornadoes and limits their destructive power (Burggraf & Foster 1977; Rotunno 2012). The structure and dynamics of these tornadoes is governed by the mixing of hot air within the core of the vortex. Artificial tornadoes within a chimney have been proposed as a way of converting green energy into electric power. But the poor understanding of the stability and mixing properties of these flows have prevented the development of an operational prototype. Vortex breakdown has also been used as a flame holder in combustion devices (Gupta *et al.* 1984), where the mixing of fuel and oxygen is of primary importance. Finally, vortex breakdown flows are of interest for bioengineering applications since they can provide a smooth and efficient mixing without moving a propeller in the cavity (Dusting *et al.* 2006; Thouas *et al.* 2007). This is beneficial for bioreactors where the growth of cells requires oxygen to be distributed as fast as possible, but where strong shears or moving objects should be avoided since they can damage cells. For such bioreactors, the goal is thus to maximize the mixing with a minimum velocity in the cavity, which will be the guiding line of the paper.

The structure and stability of a vortex breakdown flow has been actively discussed in the past century. Early experiments in a pipe (Harvey 1962; Sarpkaya 1971; Faler & Leibovich 1978) have revealed the presence of an axisymmetric bubble, which may also contain a single or a double helix (depending on the swirl and Reynolds number) with a strong hysteresis between these three regimes. The presence of the axisymmetric bubble has been explained theoretically by Benjamin (1962) and validated numerically by Wang & Rusak (1997) as a transition from a supercritical flow (without waves propagating upstream) to a subcritical flow (with waves propagating upstream) analogous to a hydraulic jump. Ruith *et al.* (2003) further showed by Direct Numerical Simulations that helical disturbances constitute a secondary instability that grow over a finite time on the axisymmetric bubble. This secondary instability can be explained by a transition from a convective to an absolute instability (Gallaire *et al.* 2006) and leads to a global mode whose structure has been described by Meliga *et al.* (2012).

Vortex breakdown has also been observed in a simpler configuration consisting of a closed cylinder with one lid rotating (Vogel 1968; Ronnenberg 1977). This is the topic of this paper since the flow is very stable experimentally. Escudier (1984) showed experimentally that vortex breakdown appears in a finite band of Reynolds number if the height to radius ratio H/R is larger than 1.5. There is a single axisymmetric bubble until $H/R = 1.95$, where a second bubble can appear and even a third one around $H/R = 3.35$. In our experiment, the aspect ratio is equal to 2 such that the flow first bifurcates toward an axisymmetric time-dependent flow at a Reynolds number around 2700. Indeed, it was found numerically by Lopez & Perry (1992) and theoretically by Gelfgat *et al.* (1996) that periodic perturbations appear, leading to a vertical oscillation of the bubble. Note however that non-axisymmetric perturbations such as a double, triple or quadruple helix may appear before the periodic perturbations, but only for aspect ratios larger than 3.3 (Gelfgat *et al.* 2001; Lopez 2006; Sorensen *et al.* 2011; Lopez 2012).

The presence of a periodic perturbation superimposed on the axisymmetric vortex breakdown is interesting because it breaks the barrier to transport. Indeed, the axisymmetric streamlines surrounding the bubble are impermeable because they connect the two hyperbolic (or heteroclinic) points located on the axis. The transport of particles from inside to outside the bubble is thus completely governed by the additional periodic perturbation. Lopez & Perry (1992) showed numerically that it advects the particles on the unstable manifold of the hyperbolic point. This is very similar to the theoretical result of Rom-Kedar *et al.* (1990) on a 2D periodic flow of two oscillating point vortices.

They showed that the particles exiting the bubble are located in the lobes between the stable and the unstable manifold of the heteroclinic points, and that the area of these lobes can be calculated by the Melnikov function. The Melnikov theory is a classical tool of dynamical systems (see e.g. Guckenheimer & Holmes 1983; Wiggins 2003) which gives a simple formula for the "distance" between the stable and the unstable manifold.

However, the barrier to transport can also be broken by a symmetry breaking, as has always been found experimentally in the steady case. Indeed, there has been a long debate on the structure of vortex breakdown since it was different depending on whether it was predicted by axisymmetric numerical simulations or observed in the experiments that revealed asymmetric tongues of dye exiting from the bubble due to what was thought to be an intrinsic asymmetry of the bubble (Spohn *et al.* 1998). It was finally proven (Thompson & Hourigan 2003) that these tongues can be due to very small imperfections of the experimental set-up, since a misalignment of $0.01°$ of the rotation axis (which is of course inevitable) is sufficient to recover the large asymetries observed in the experimental images. This phenomenon highlights the high sensitivity of the flow to asymetries, which will be introduced on purpose in this paper in order to quantify their effect on the mixing. Sotiropoulos *et al.* (2001) showed numerically that it creates a rich dynamics such as KAM tori and stable islands inside the bubble, which have even been observed in experimental Poincaré sections (Sotiropoulos *et al.* 2002; Fountain *et al.* 1998). They also showed that the stretching and folding of the lobes creates a cantorus at the periphery of the bubble, which is responsible for a chaotic release of the particles initially located inside the bubble. This leads to a devil's staircase (with fractal steps) for the number of particles as a function of time. This has been confirmed by Brons *et al.* (2007) who also noted that the asymmetry can be reduced by introducing a small offset of the axis of the rotating lid to counter-balance its misalignment. However, there has never been a quantitative prediction of the escape rate from the bubble, as was done in Rom-Kedar *et al.* (1990). Moreover, all these studies only analyze the evolution of point tracers (position, spatial structure, fractal dimension...). They have always neglected the effect of diffusion which is able to break the barrier to transport and introduce a weak escape rate predicted theoretically by Brons *et al.* (2009).

By contrast, many studies have been devoted to the advection-diffusion of a scalar in a homogeneous turbulent flow (see e.g. the review of Warhaft 2000). The goal is to derive the spectra, the Probability Distribution Functions (PDF) and the variance of the scalar. In the inertial range the spectra scale as $k^{-5/3}$ but they scale as k^{-1} at smaller scales (between the Kolmogorov and the Batchelor scale), as explained by Batchelor (1959) and Kalda (2000) in a stationary regime. The PDF reveal a high intermittency (non Gaussian), which can be explained by a simple model of stretched filaments (Duplat & Villermaux 2008; Meunier & Villermaux 2010). However, the most important result is probably the fact that the variance decays exponentially, as was shown numerically in a 2D almost time-periodic flow (Pierrehumbert 1994; Antonsen *et al.* 1996; Thiffeault *et al.* 2004; Meunier & Villermaux 2010) and in a 3D flow (Toussaint *et al.* 1995). This can be explained in a bounded domain by the linearity of the advection-diffusion equation (Haynes & Vanneste 2005). However, Gouillart *et al.* (2007) showed experimentally that the walls can have a non-trivial effect and lead to "anomalous" power law rather than an exponential decay.

In this paper, we will study experimentally the mixing inside a highly heterogeneous flow. Section 2 is devoted to the experimental set-up. The flow is described in detail in section 3. The mixing properties of the flow are studied in the absence of vortex breakdown in section 4, and in the presence of vortex breakdown in section 5. Conclusions follow in section 6.
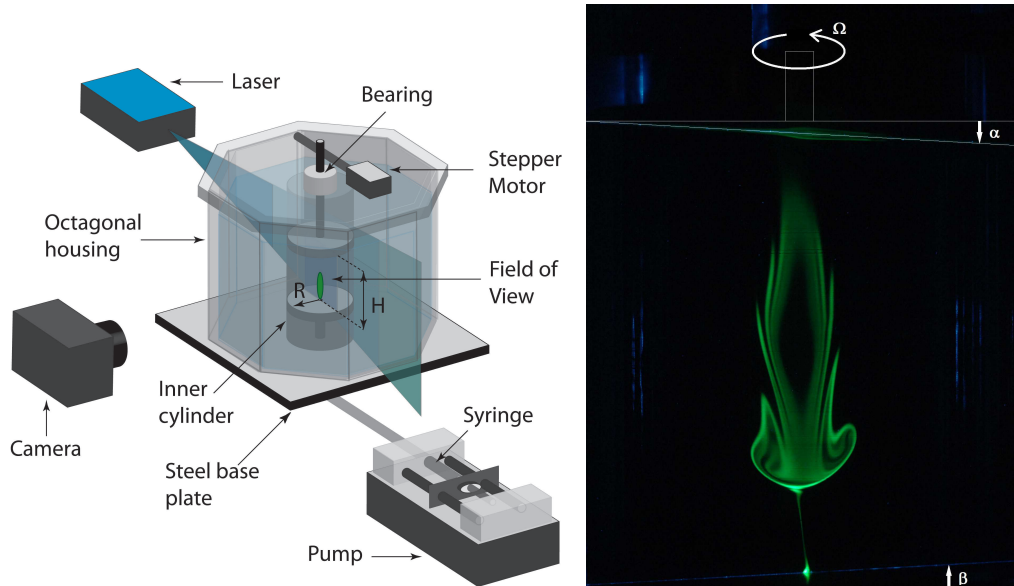
FIGURE 1. Schematic of the experimental set up.

2. Materials and methods

2.1. *Experimental setup*

We wish to study the flow inside a circular cylinder with a rotating tilted disk. The set-up has been described in detail in Ismadi *et al.* (2011) and will only be presented briefly here. Figure 1 shows the experimental set-up, consisting of a cylindrical Plexiglas container with internal radius $R = 32.5$mm, filled with water. This inner cylinder is placed inside an octagonal housing full of water with flat exterior faces to prevent the deformation of images. The flow under study is located inside the inner cylinder between two disks separated by a height H, with an aspect ratio $H/R = 2 \pm 1\%$. The top disk is rotated at an angular velocity Ω varying from 0.6 to 3.6 rad/s using a stepper motor and a worm wheel allowing a very smooth rotation of the disk at all speeds.

The goal of the paper is to study the mixing properties of the flow inside the inner cylinder. For this purpose, a dye mixture is injected at the centre of the bottom disk through a 0.5mm hole connected to a 1ml syringe. A syringe pump creates a continuous injection at a volumetric flow rate $Q = 0.02$ ml/min for 5 minutes. This duration of injection was chosen because it is small compared to the typical time of the experiments (of the order of a few hours) needed for the dye to spread within the whole cylinder. But this duration is long enough for the velocity of the injection jet (0.17cm/s) to be small compared to the velocity of the disk periphery varying from 2 to 12cm/s. The injected volume (0.1ml) is, of course, very small compared to the total volume of the cylinder (200ml). The mixture contains 0.033% of Fluorescein in weight diluted in water, together with 0.088% of alcohol in order to obtain a neutrally buoyant mixture. Indeed, Ismadi *et al.* (2011) showed that a weak density difference of the order of 0.01% is sufficient to modify the threshold of the vortex breakdown.

The Fluorescein dye is illuminated by a blue laser so that it fluoresces very brightly with a green color. As illustrated in Figure 1(a), the laser is expanded into a vertical sheet that is carefully placed at the centre of the inner cylinder to visualise the distribution of dye in a longitudinal section. A digital camera records images similar to the one shown

in Fig. 1(b). Although the blue component of the images contains strong reflections of the laser sheet, the green component only contains the image of the dye and its intensity is proportional to the density of the dye at this high dilution rate.

As will be shown later, the mixing properties of this flow strongly depend on the asymmetries of the experiment. We have thus tested two types of asymmetries: a tilt of the rotating disk and a tilt of the stationary disk. As shown in Fig. 1(b), the tilt of the rotating disk is obtained by cutting the disk at an angle α compared with the plane normal to the axis of the disk. This creates an oscillating motion of the periphery (in a given section) superimposed on the rotation of the disk. This does not correspond to the motion of a disk whose axis is tilted with respect to the axis of the cylinder. Six different disks with angles α equal to 0, 2, 5, 7.2, 9.8 and 14.6 degrees have been used, with an accuracy of less than 0.1 degree. The tilt of the stationary disk is obtained by placing a thin disk on a wedge at an angle β, which is varied from -2.6 to 2.6 degrees. The uncertainty on the angle β is relatively large even in the absence of a wedge.

The flow is also studied using Particle Image Velocimetry (PIV), by injecting small red fluorescent particles in the cylinder. A 4 mega-pixels PIV camera acquires images through a red filter in order to remove reflections of the laser. The images are treated using an inhouse cross-correlation algorithm (Meunier & Leweke 2003), which gives 60 by 60 vectors in the longitudinal section. The acquisition frequency is equal to 8 times the rotation frequency of the top disk in order to apply some phase averaging of the velocity fields.

2.2. *Theoretical and numerical formulation*

The flow under consideration depends on four main dimensionless parameters. The aspect ratio $h = H/R$ is kept to a constant value of 2. The Reynolds number $Re = \Omega R^2/\nu$, ν being the kinematic viscosity of the water, is varied between 700 and 3000. The angle α of the tilted rotating disk is varied between 0 and 15 degrees. The angle β of the stationary disk is varied between -2.6 and 2.6 degrees in the plane normal to the laser sheet. The Schmidt number $Sc = \nu/\kappa$ (κ being the diffusivity of the dye) is an additional parameter which is large in the experiment and equal to 2000.

The flow is governed by the Navier-Stokes equation together with the incompressibility condition, which are non-dimensionalised using the radius R and Ω^{-1} as length and time scales, leading to

$$\frac{\partial \boldsymbol{u}}{\partial t} + \boldsymbol{u} \cdot \nabla \boldsymbol{u} = -\nabla p + \frac{1}{Re}\triangle \boldsymbol{u}. \tag{2.1}$$

In cylindrical coordinates (r, θ, z), the boundary conditions are $\boldsymbol{u} = 0$ at the periphery ($r = 1$) and at the bottom disk ($z = \beta r \cos(\theta)$) and $\boldsymbol{u} = r\mathbf{e}_\theta$ (where $\mathbf{e}_\theta$ is the orthoradial unit vector) on the top disk defined by $z = h + \alpha r \cos(\theta - t)$.

These equations are easily solved numerically at these moderate Reynolds numbers using Comsol Multiphysics which is a finite element method using standard Lagrange elements P1-P1. The time-stepping is governed by an IDA solver (Implicit Differential-Algebraic) based on a BDF scheme (Backward Differentiation Formula) described by Hindmarsh *et al.* (2005). At each time step, the system is solved using the direct linear solver for hollow matrices-Pardiso (www.pardiso-project.org). The flow is first calculated as a time dependent flow from $t = 0$ to $t = 100$, with $\boldsymbol{u} = 0$ at $t = 0$. The solution at $t = 100$ is then used as an initial condition for a stationary solver. The mesh is refined in the boundary layer, leading to 14,882 elements in 2D and 511,000 elements in 3D.

The concentration of the dye is a passive scalar c advected by the flow according to

the linear diffusion-advection equation

$$\frac{\partial c}{\partial t} + \boldsymbol{u} \cdot \nabla c = \frac{1}{ReSc} \triangle c, \qquad (2.2)$$

This equation is not solved numerically because the Schmidt number is large such that dye structures are very thin. The calculation would need an increased spatial resolution at his large Peclet number ($Pe = ReSc \simeq 10^6$), which would be very difficult in 3D. This is why the numerical simulations are only used to derive the characteristics of the flow and not to study the mixing problem itself.

3. Phenomenology of the flow

We first describe the helical flow inside the cylinder with a rotating disk, which is well known to exhibit vortex breakdown. The effect of the tilt of the rotating disk is analysed in detail to explain the mixing properties of this flow in the next sections.

3.1. *Vortex breakdown in the presence of a tilted disk*

The rotation of the top disk creates a thin rotating layer below the disk, which induces a radial motion due to the centrifugal force. This Von Karman pumping creates a secondary longitudinal recirculation inside the cylinder, which is very well visualised at moderate Reynolds number (see Fig.2a) by the dye going up along the axis of the cylinder. This toroidal motion is very weakly affected by the tilt of the disk, which creates a weak periodic perturbation leading to a small undulation of the dye streakline below the top disk. The dye accumulates on the top disk and is then advected radially toward the corners by the centrifugal motion. At the corners, the dye predominantly goes down along the periphery of the cylinder due to the recirculation. But a small part is ejected radially inward due to small peripheral jets, which will be analysed in detail in section 3.3.

When the Reynolds number increases, the undulation of the streakline on the axis increases because the upward velocity decreases on the axis. At the critical Reynolds number where the velocity vanishes on the axis, the topology of the flow suddenly changes. This leads to the well-known vortex breakdown bubble, clearly visualised in Fig. 2(b). Here, the aspect ratio h is equal to 2 such that the critical Reynolds number is equal to $Re = 1430 \pm 30$, in excellent agreement with the literature (see Escudier 1984). This critical Reynolds number is very weakly affected by the tilt of the disk: it seems to decrease by 20 due to the tilt of the disk, although this could be within the uncertainty.

Figure 2(c) shows that for a larger Reynolds number ($Re = 1900$), the vortex breakdown is larger and contains two bubbles. However, when the Reynolds number is increased further, the size of the bubble decreases and the bubble eventually disappears above $Re = 3000 \pm 50$, as shown on Fig. 2(d). This is again in excellent agreement with the results of the literature obtained in the absence of tilt. It can be noted that the tilt of the disk creates a small undulation of the streakline just above the bottom disk, at the location where the bubble disappeared (i.e., where the vertical velocity is minimum).

3.2. *Potential flow induced by the tilted disk*

PIV measurements have been performed in order to quantify the meridional flow. Figure 3(a) shows the mean flow in a vertical section in the absence of vortex breakdown. The velocity field clearly shows the axisymmetric recirculation with a strong upward flow on the axis and a downward flow at the periphery. It can be noted that the radial flow is thinner and stronger at the top than at the bottom because it is contained within the layer.
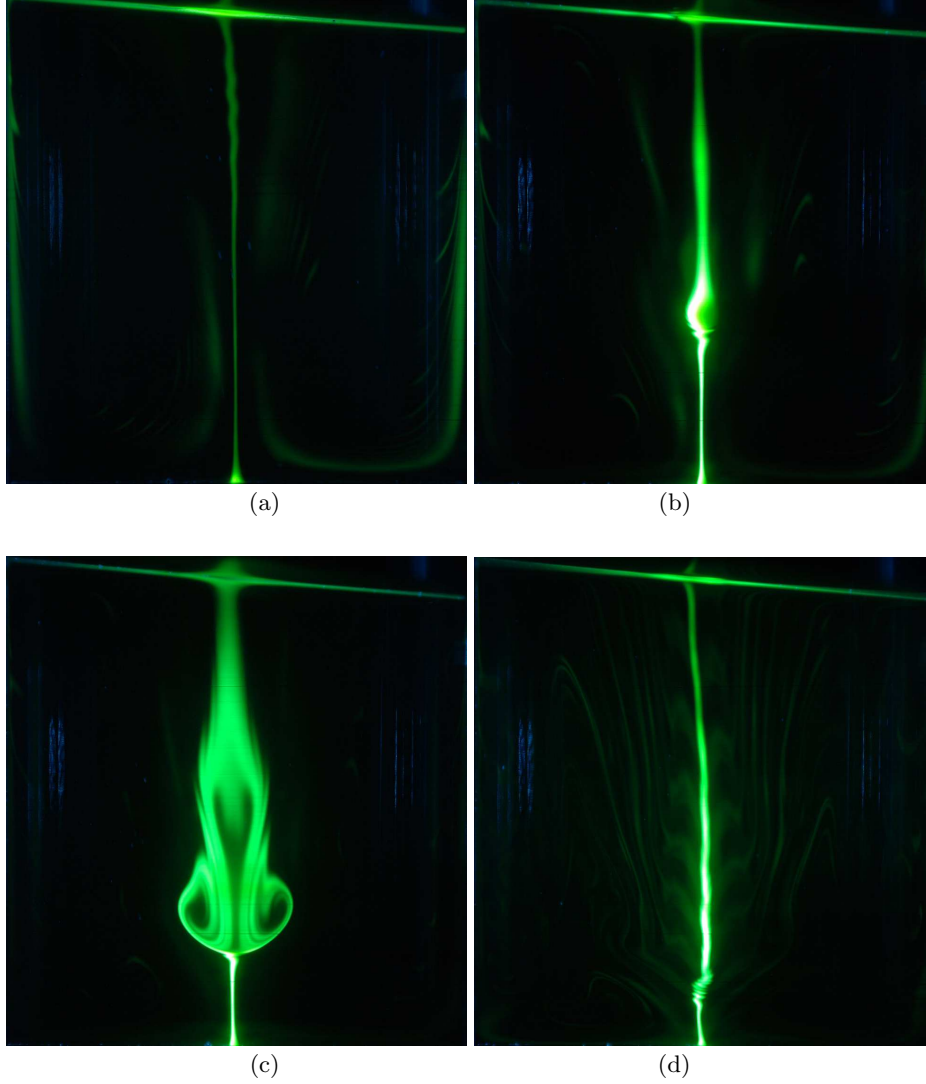
FIGURE 2. Dye visualisation of the flow inside the cavity at the end of the injection phase. (a) $Re = 1000$, (b) $Re = 1470$, (c) $Re = 1900$ and (d) $Re = 3500$. $\alpha = 5°$, $h = 2$.

The periodic perturbation due to the tilt of the disk can be measured by calculating the difference between the phase averaged velocity and the mean velocity. This perturbation is plotted in Fig. 3(b) in the absence of vortex breakdown. It is clear that there is a strong flow from right to left, due to the tilted disk which pushes the fluid as it rotates. This flow is mainly potential because it is created by the motion of the disk normal to its surface. It can thus be calculated using the theory for potential flows, by assuming that the velocity $\boldsymbol{u} = \nabla\varphi$ derives from the potential function φ. The potential function φ is searched as a sum of potential modes of amplitude a_n:

$$\varphi = \alpha \sum_n \frac{a_n}{k_n} \cosh(k_n z) \cos(\theta - t) J_1(k_n r), \tag{3.1}$$

where J_1 is the Bessel function of the first kind. Each mode is indeed a solution at any time because it satisfies $\nabla \boldsymbol{u} = \triangle\varphi = 0$. The slip boundary condition ($u_r = 0$) at the
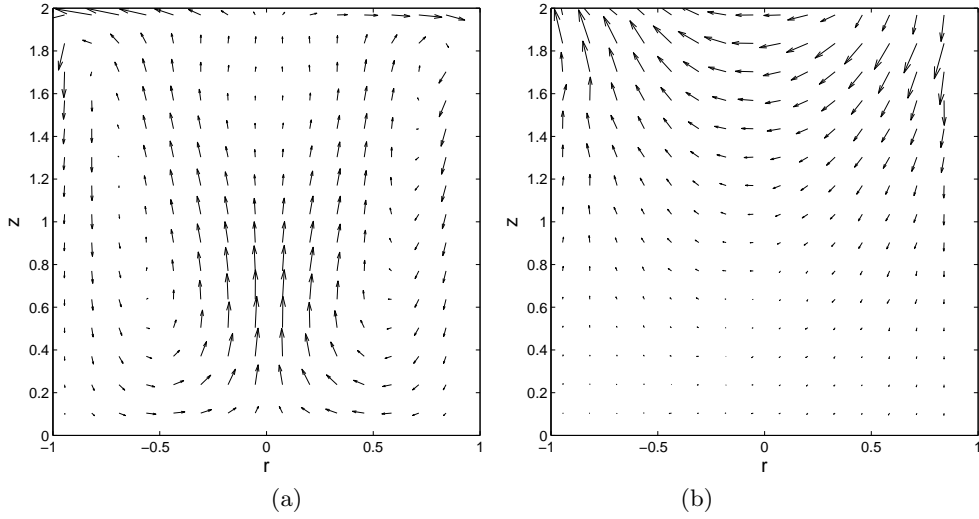
FIGURE 3. (a) Mean flow and (b) periodic perturbation flow obtained by PIV in a longitudinal section perpendicular to the plane of the tilt angle. $Re = 1000$, $\alpha = 5°$, $h = 2$

periphery ($r = 1$) imposes the choice of the axial wavenumber k_n

$$J_1'(k_n) = 0, \tag{3.2}$$

such that there is a discrete set of wavenumbers, whose first terms are equal to $k_1 = 1.8412$, $k_2 = 5.3314$, $k_3 = 11.7060$ and $k_4 = 14.863$. The slip boundary condition at the tilted disk can be written:

$$u_z = \alpha r \cos(\theta - t) \quad \text{at} \quad z = h - \alpha r \sin(\theta - t). \tag{3.3}$$

This slip boundary condition is *a priori* valid only when the thickness δ of the boundary layer (which scales as $Re^{-1/2}$) is much smaller than the vertical displacement of the tilted disk (which is equal to α at $r = 1$), i.e., when $\alpha Re^{1/2} \gg 1$. However, it is also valid when $\alpha Re^{1/2} \ll 1$ because in the frame of reference precessing with the disk (i.e., with the z axis normal to the disk), the Poincaré force is of order α and is thus negligible compared to the viscous terms governing the boundary layer which are of order $Re^{1/2}$. In this frame of reference, the boundary layer is thus axisymmetric, meaning that the thickness δ is independent of θ, such that the slip boundary condition (3.3) is still valid but at a distance δ below the disk, i.e., at $z = h - \alpha r \sin(\theta - t) - \delta$.

Since δ and α are small in both cases, the boundary condition can be replaced at leading order by the same condition applied at $z = h$:

$$u_z = \alpha r \cos(\theta - t) \quad \text{at} \quad z = h, \tag{3.4}$$

A solvability condition is then found by introducing the decomposition (3.1) into this boundary condition, multiplying by $rJ_1(k_m r)$, and integrating r from 0 to 1 because $\int_0^1 J_1(k_n r) J_1(k_m r) r dr = 0$ if n and m are not equal. This leads to the value of the amplitude a_n which can be simplified as

$$a_n = \frac{\int_0^1 J_1(k_n r) r^2 dr}{\int_0^1 J_1^2(k_n r) r dr \sinh(k_n h)} = \frac{2}{k_n J_0(k_n)(k_n^2 - 1) \sinh(k_n h)}. \tag{3.5}$$
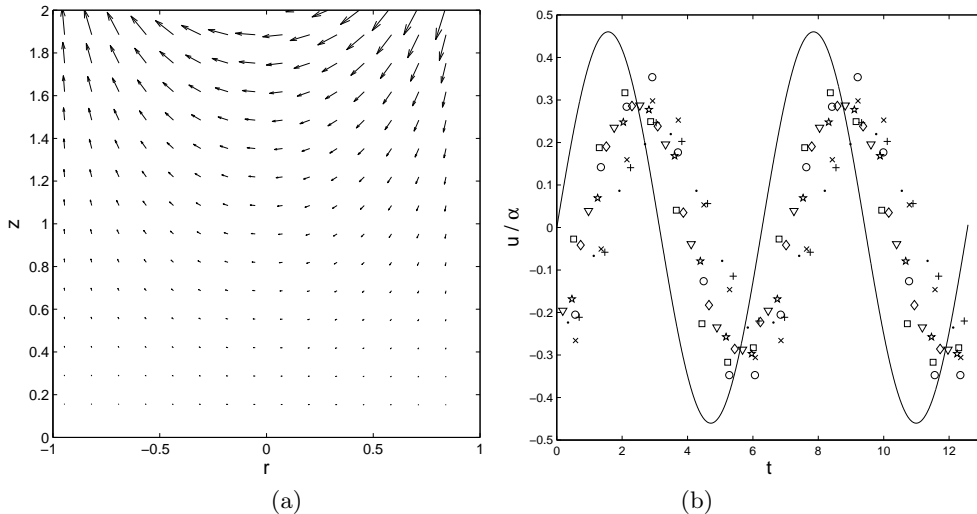
FIGURE 4. (a) Periodic potential flow obtained theoretically using (3.6). (b) Amplitude of the periodic flow on the axis at $z = 1.8$ obtained experimentally at $Re = 1000$ ($\bullet$), $Re = 1255$ ($\circ$), $Re = 1490$ ($\times$), $Re = 1750$ ($\square$), $Re = 2000$ ($\star$), $Re = 2250$ ($+$), $Re = 2490$ ($\diamond$) and $Re = 3036$ ($\triangledown$). $\alpha = 5°$ and $h = 2$.

The velocity is obtained by differentiating (3.1):

$$\boldsymbol{u} = \sum_n a_n \begin{pmatrix} J_1'(k_n r) \cosh(k_n z) \cos(\theta - t) \\ -J_1(k_n r) \cosh(k_n z) \sin(\theta - t)/(k_n r) \\ J_1(k_n r) \sinh(k_n z) \cos(\theta - t) \end{pmatrix}. \tag{3.6}$$

This velocity field is plotted in Fig. 4(a) and is similar to the perturbation field found experimentally and plotted in Fig. 3(b). Moreover, there is a good quantitative agreement of the amplitude of the flow, as shown in Fig. 4(b) where the radial velocity on the axis is plotted as a function of time. The experimental result clearly shows that the potential flow is independent of the Reynolds number. However, it seems that the experimental velocity is slightly delayed compared to the theoretical prediction. This may be due to nonlinear effects inside the boundary layer, which have not been taken into account here.

3.3. *Peripheral jets induced by the tilted disk*

As shown on Fig. 5(a), the perturbation flow (i.e. the difference between the phase-averaged flow and the mean flow) contains almost no vorticity in the bulk of the cylinder, because the potential flow calculated in the previous section is irrotational. However, there is some vorticity created at the top disk which is advected to the periphery of the cylinder. It should be noted that this periodic vorticity perturbation is small compared with the mean distribution of vorticity (not shown here). The mean vorticity is antisymmetric whereas the periodic perturbation is symmetric. At the periphery, this symmetric vorticity corresponds to two helical vortices of opposite sign which are advected downward by the mean flow. These vortices are due to the oscillating motion of the disk at the corner, which creates some oscillating vorticity.

These counter-rotating vortices create small radial jets which are responsible for the tongues of dye which are visible in Fig. 2(a). The radial velocity of these jets is plotted as a function of z close to the cylinder in Fig. 5(b). It seems that the wavelength of the undulations (i.e. the pitch of the helical vortices) is independent of the Reynolds

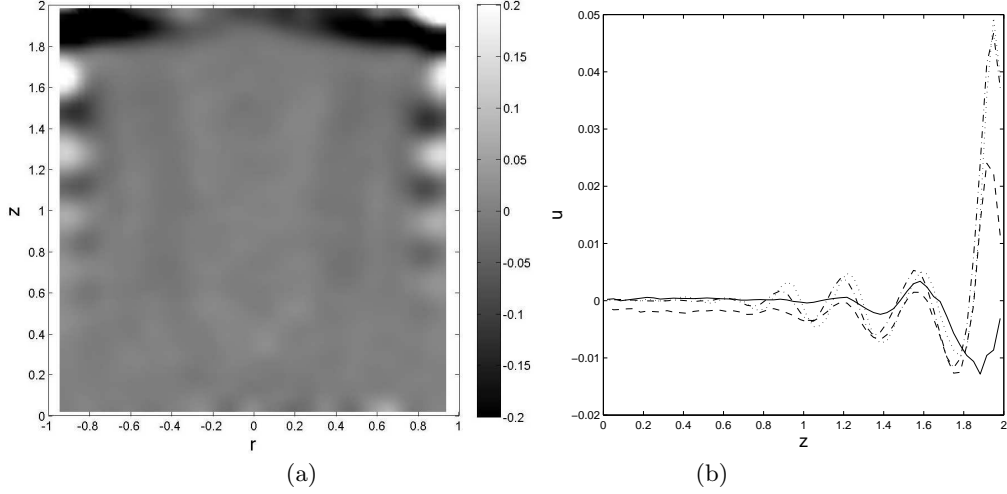(a)   (b)

FIGURE 5. (a) Periodic perturbation vorticity obtained by PIV at $Re = 2000$. (b) Vertical profile of radial velocity at $r = 0.9$ obtained experimentally at $Re = 1000$ (solid line), $Re = 1490$ (dashed line), $Re = 2000$ (dash-dotted line) and $Re = 2490$ (dotted line). $\alpha = 5°$, $h = 2$.

number and equal to 0.35. This is close to the value $2\pi u_z^{\mathrm{max}} = 0.38$ of a perturbation at a frequency $1/2\pi$ advected by the mean flow at the velocity u_z^{max} (which is found empirically to be constant around 0.06 for $Re \in [500, 3500]$).

The strength of these jets decreases when the vortices are advected downwards due to viscous diffusion. Indeed, the attenuation is stronger at smaller Reynolds numbers: the oscillations disappear after 2 wavelengths at $Re = 1000$ whereas they are still visible after 4 wavelengths at $Re = 2490$. Despite the large uncertainty in the measurement, it is possible to fit the envelope of these oscillations by a decaying function of the form:

$$u_r^{\mathrm{envelope}} = u_r^{\mathrm{max}} e^{\mu(z-h)} \tag{3.7}$$

The attenuation parameter μ is plotted in Fig. 6(a) as a function of the Reynolds number for 3 different tilt angles. It is quite clear that this parameter is fairly independent of the tilt angle α and decreases with the Reynolds number approximately as $Re^{-1/2}$. This is coherent with the fact that these jets extend on a larger height when the Reynolds number increases. The amplitude of these jets is characterized by u_r^{max} in (3.7) which is plotted in Fig. 6(b). It is surprising to see that the amplitude decreases with the Reynolds number. This is probably due to the fact that these jets come from an interaction of the viscous boundary layer (of thickness $Re^{-1/2}$) with the tilt angle α. This would explain why the amplitude scales as $\alpha Re^{-1/2}$. Using these two empirical laws, it is possible to give a general formula for the radial velocity of these jets at $r = 0.9$:

$$u_r(\theta, z, t) = 15\alpha Re^{-1/2} \exp[100 Re^{-1/2}(z-h)] \sin[18(z-h) + \theta - t] \tag{3.8}$$

where α is given in radians. This empirical formula will be used in the following.

To summarize, the presence of a tilt of the rotating disk does not modify drastically the mean flow, including the vortex breakdown bubble. However, it leads to a periodic potential flow in the bulk of the cylinder and creates periodic radial jets at the top corners which are advected downward by the mean flow.
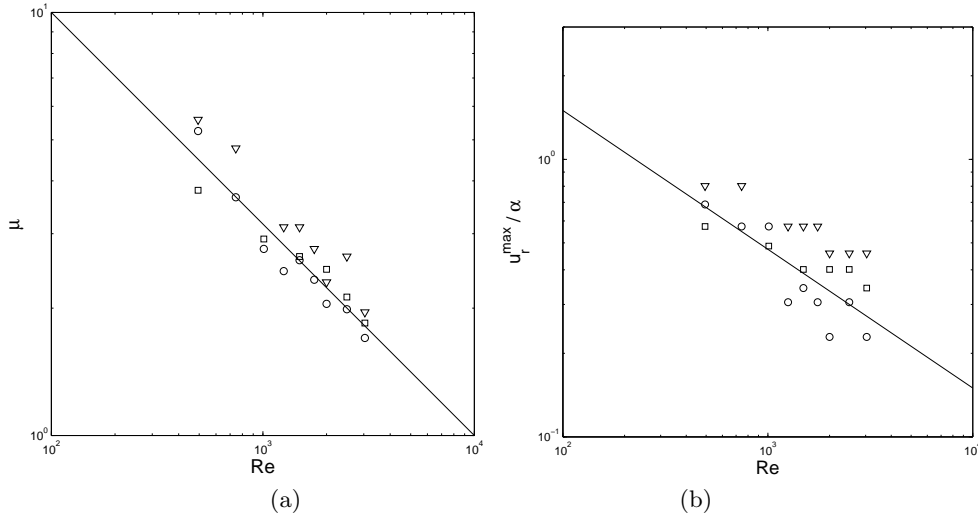
FIGURE 6. (a) Attenuation parameter μ and (b) amplitude $u_{\max}$ used to fit the envelope of the radial velocity at $r = 0.9$ using (3.7). Tilt angles are equal to $\alpha = 5°$ ($\triangledown$), $\alpha = 10°$ ($\square$) and $\alpha = 15°$ ($\circ$).

4. Mixing in the absence of vortex breakdown

4.1. *Mixing for a flat disk*

Figure 7 shows the temporal evolution of the dye after injection on a long term. The dye is advected by the meridional recirculation on a torus and is thus homogeneous along the streamlines. The dye is mainly located on the axis, with a thickness which increases with time. This indicates that there is some diffusion across the streamlines, which allows to spread the dye over the whole volume and thus to decrease the intensity of the dye. However, this effect is weak because the dye is still inhomogeneous at $t = 4000$ (i.e. after 1 hour of experiment), as shown by Fig. 7(d) where the dye is located on the axis and at the walls. This leaves a large region without any dye, indicating that this flow is fairly inefficient for mixing.

In fact, there is a small asymmetry in the dye pattern (particularly visible on the axis of Fig. 7a), which is due to small imperfections in the experimental setup. This alternate chevron pattern is probably due to a non-zero angle β because this asymmetry is stationary with time. It is probably this asymmetry which creates a diffusion across the streamlines rather than the molecular diffusion whose characteristic time is equal to the Péclet number ($Pe = ReSc \sim 10^6$) in non-dimensional units. This already shows that the mixing properties of this flow are highly dependent on the possible asymmetries of the flow.

4.2. *Mixing for a tilted disk*

To study quantitatively the effect of the asymmetry, the rotating disk is tilted of an angle $\alpha = 5°$ to surpass the effect of the imperfections of the set-up. Fig. 8 shows the temporal evolution of the dye at the same instants in time. The dye is still advected by the meridional recirculation, leading to a dense region of dye on the axis. However, the diffusion across streamlines is much faster, as the dye has spread over the whole volume at $t = 1000$ and is completely homogeneous at $t = 4000$.

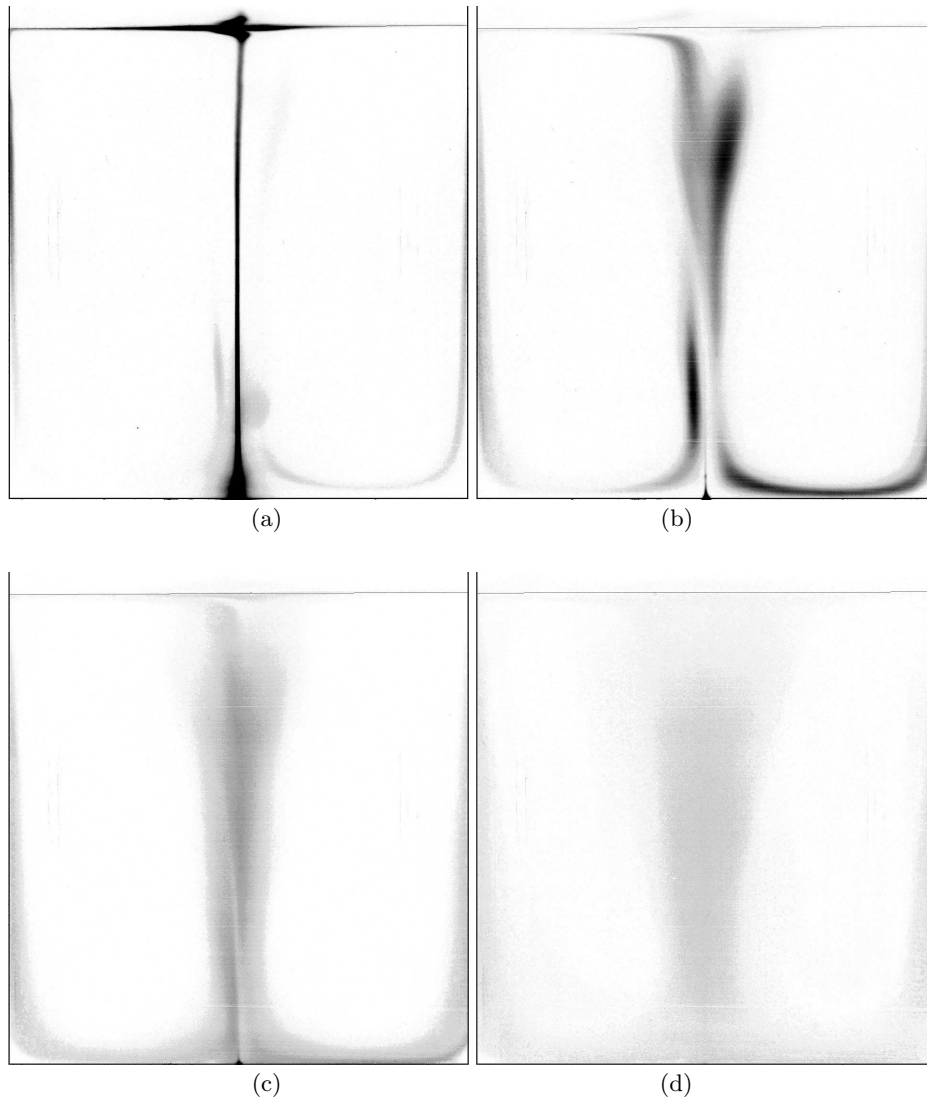This enhanced mixing is due to the tongues of dye which appear on the lateral walls

FIGURE 7. Dye visualisation at $t = 0, 300, 1000, 4000$. $Re = 1000$, $\alpha = 0°$. (negative image of the green component)

due to the radial jets created at the top corners and advected along these walls (see section3.3). These tongues are advected by the flow to fill the bulk of the cylinder, leading to a rapid homogenization of the dye within the whole cylinder. This is clearly visible in 8(b).

4.3. *Homogenization time*

The mixing efficiency of the flow can be studied quantitatively by comparing the Probability Density Function (PDF) of dye concentration for two different tilt angles. These PDF are homothetic to the PDF of intensity $P(I)$ (i.e. the normalized number of pixels with an intensity I) which are plotted in Fig. 9(a) because the dye concentration c is proportional to the image intensity I. For $\alpha = 0$, the PDF contains a high and narrow peak at $I = 10$ corresponding to the regions without dye. But there is also a small and
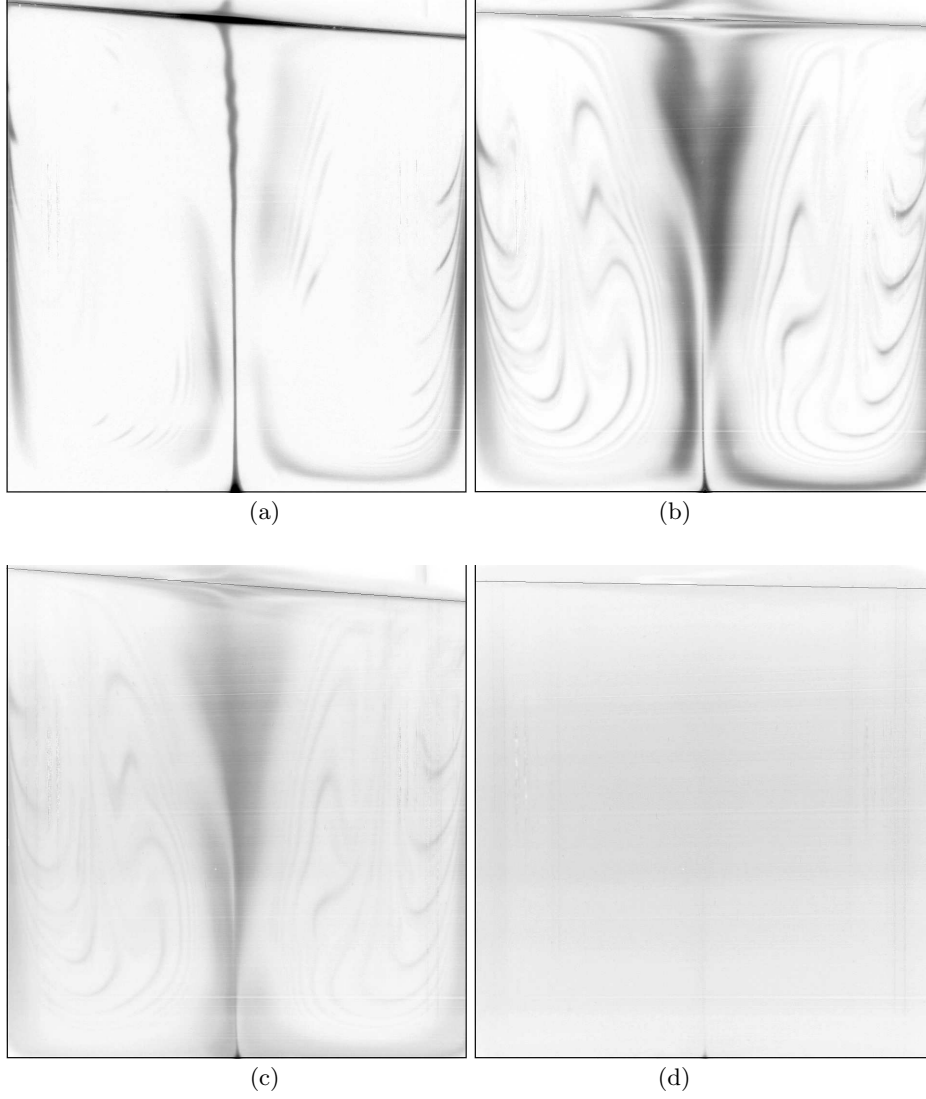
FIGURE 8. Dye visualisation at $t = 0, 300, 1000, 4000$. $Re = 1000$, $\alpha = 5°$. (negative image of the green component)

broad peak at $I = 200$ corresponding to the region around the axis with a lot of dye. These two peaks are separated by a large plateau indicating the inhomogeneity of the dye within the volume. For $\alpha = 5°$, at the same time, there is a single peak at $I \sim 100$ which indicates that all parts of the cylinder have almost the same concentration of dye, which is the sign of a mixed state.

As time evolves, each PDF changes from two separated peaks (at 0 and at the initial injection concentration) to a single peak at the mean final concentration. The mixing is thus well characterized by the broadness of the PDF, i.e. the standard deviation σ of the intensity defined by

$$\sigma^2 = \langle (I - \langle I \rangle)^2 \rangle = \int I^2 P(I) dI - \left[\int I P(I) dI \right]^2 \tag{4.1}$$
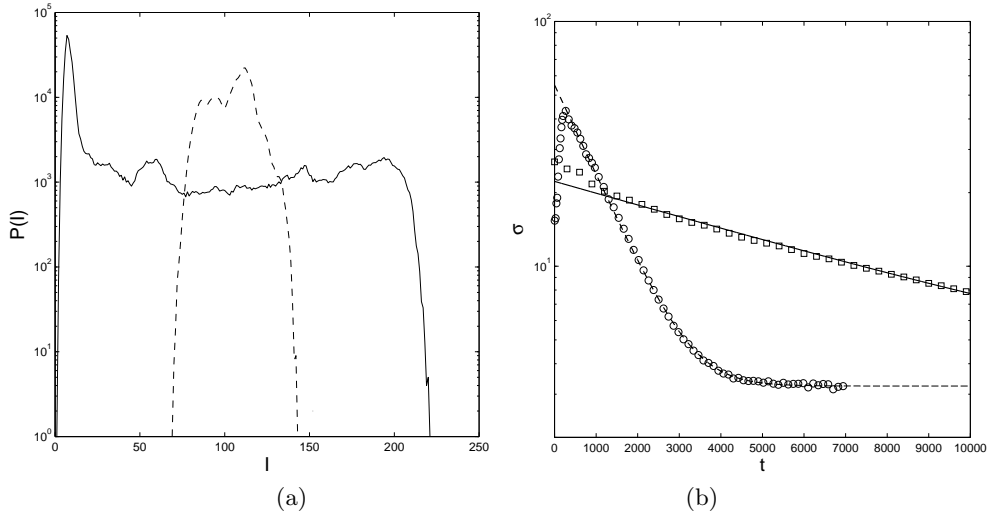
FIGURE 9. (a) PDF of the intensity of the images at $t = 3200$ for $\alpha = 0°$ (solid line) and $\alpha = 5°$ (dashed line). (b) Temporal variation of the variance of the image intensity σ for $\alpha = 0°$ ($\triangle$) and $\alpha = 5°$ ($\circ$). Lines correspond to the fit (4.2). $Re = 1000$.

where $\langle \cdot \rangle$ denotes the spatial average for $r < 0.6$ and $z \in [0.1; 1.9]$. The evolution of the standard deviation is plotted in Fig. 9(b) for two different tilt angles. It is clear that it decays exponentially in both cases after a small transient stage (although there is a saturation of the standard deviation at late stages for $\alpha = 5°$, due to the noise in the measurements). It is also clear that the decaying of the standard deviation is much faster for $\alpha = 5°$ than for $\alpha = 0$, which proves quantitatively that the mixing is strongly enhanced by the tilted disk.

The decay of the standard deviation is very well fitted by a law

$$\sigma^2(t) = \sigma_0^2 e^{-2t/T} + \sigma_{\text{noise}}^2 \tag{4.2}$$

which is plotted as lines on Fig. 9(b). This allows to measure accurately the homogenization time T (i.e. the decaying time of the standard deviation) for any experiment. It should be noted that this homogenization time does not depend on the amount of dye injected (which only modifies the multiplying factor σ_0). It was also checked that it is independent of the region taken to make the spatial average at late stages. This can be understood by the fact that the dye concentration c is solution of a linear equation (2.2) which admits at any time an infinite set of eigen modes $c_n(r)$. For $\alpha = 0$, the flow is stationary such that it is the same eigen mode at any time and the solution can be written:

$$c(\mathbf{r}, t) = \sum A_n c_n(\mathbf{r}) e^{-t/T_n} \tag{4.3}$$

where $-1/T_n$ is the eigenvalue of the mode and A_n is the amplitude of the mode at $t = 0$, which is given by the initial condition $c(\mathbf{r}, 0) = \sum A_n c_n(\mathbf{r})$. It should be noted that T_n is always positive because it is a diffusive process; it is actually equal to $2 ReSc \int c_n(r)^2 d\mathbf{r} / \int |\nabla c_n(r)|^2 d\mathbf{r}$ (see e.g. Toussaint $et\ al.$ 2000). In an infinite medium, there is an infinite number of eigenvalues such that T_n may not be bounded. This is the case, for example, in the absence of velocity where a blob of scalar converges to a Gaussian distribution whose variance decays as $1/t$ and not exponentially. However, in a confined geometry, the small-scale cutoff imposed by diffusivity reduces the problem to
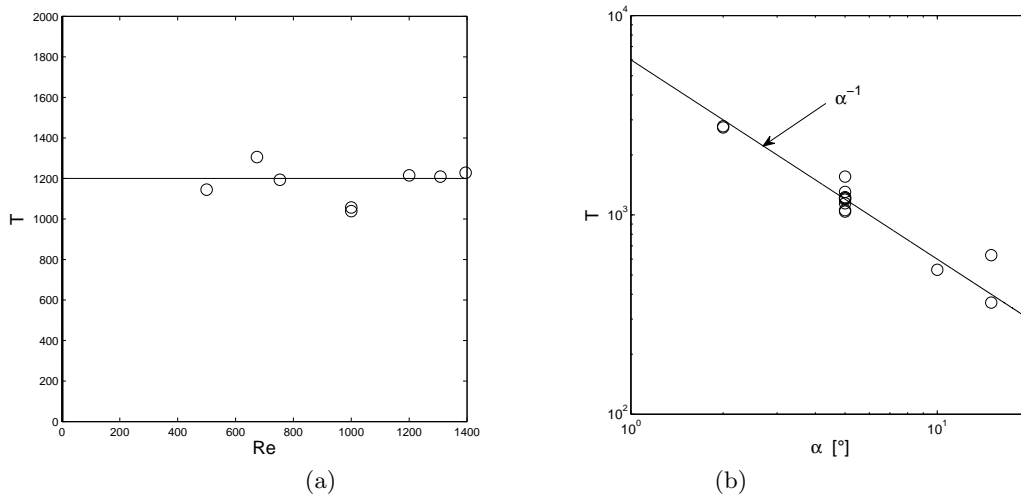
FIGURE 10. Decaying time as a function of (a) the Reynolds number at $\alpha = 5°$ and (b) as a function of the tilt angle α for all Reynolds number without vortex breakdown.

a finite-dimensional system, at least for 2D flows (Haynes & Vanneste 2005). This permits one to define the maximum decaying time T_1, which corresponds to the dominant mode remaining at late stages since it is the least damped mode. This means that at late stages, σ is equal to the standard deviation of $c_1(r)$ over the region considered for the treatment of the images multiplied by $A_1 e^{-t/T_1}$ (if $A_1 \neq 0$). This demonstrates that the homogenization time T is independent of the region considered (unless $c_1(r)$ vanishes on this region). It also explains why the standard deviation σ decreases exponentially. For $\alpha \neq 0$, the flow is not stationary but periodic. The same analysis can be done over each period, such that the result is still valid for integer values of time. The standard deviation is thus an exponential decay multiplied by a periodic function and $-1/T_1$ corresponds to the Floquet multiplier.

The homogenization time T is plotted in Fig. 10(a) as a function of the Reynolds number in the absence of vortex breakdown. It seems fairly constant around 1200 for a tilt angle $\alpha = 5°$. This can be understood by the fact that the radial jets are stronger but are damped quicker at smaller Reynolds numbers. These two effects annihilate each other which leads to the independence of T with respect to Re.

The homogenization time is plotted in Fig. 10(b) as a function of the tilt angle α for all Reynolds numbers (without vortex breakdown). It is clearly decreasing as a function of α, and seems to be well fitted to by a law scaling as α^{-1}. This shows that the homogenization time of this flow is strongly dependent on the tilt angle of the rotating disk. But it poses a problem for the axisymmetric configuration with $\alpha = 0$. In fact, the homogenization time T saturates probably due to small imperfections in the symmetry of the set-up or at least due to the molecular diffusion which gives an upper bound equal to the Péclet number (Pe $\sim 10^6$ at these Reynolds and Schmidt numbers).

4.4. A simple model

It is possible to give an estimate of the homogenization time by calculating the amount of concentrated dye which is ejected from the periphery to the bulk of the cylinder due to the radial jets. Using the empirical formula (3.8) of the radial velocity, the inward flux

of fluid going from the periphery to the bulk can be calculated at $r = 0.9$ as

$$\Phi = \int_{z=0}^{z=h} \max(-u_r, 0) r d\theta dz \simeq 0.27\alpha(1 - e^{-100Re^{-1/2}h}) \qquad (4.4)$$

This is valid for large Reynolds numbers when the radial jets are attenuated on a length larger than the wavelength of the oscillation. Furthermore, when h is larger than $Re^{1/2}/100 \simeq 0.3$, the flux becomes independent of the Reynolds number, equal to $0.27\,\alpha$. This explains why the homogenization time T is independent of the Reynolds number. This flux creates an exchange between the volume V_p of the periphery at the concentration c_p and the bulk with a volume V_b at the concentration c_b. It leads to two coupled equations for c_p and c_b, whose solutions are exponentially decaying toward the mean concentration with a characteristic time:

$$T = \frac{V_b V_p}{\Phi(V_b + V_p)} \simeq \frac{1.8h}{\alpha} \qquad (4.5)$$

Here, $V_b = 0.81\pi h$ and $V_p = 0.19\pi h$ correspond to the volumes inside and outside $r = 0.9$, and α is given in radians. This gives a correct scaling law for the homogenization time as α^{-1} but this prediction is 30 times below the experimental measurement plotted in Fig. 10(b).

It should be noted that the theory depends on the choice of the radius r at which the flux is evaluated. However, when r is close to the cylinder, the radial velocity vanishes such that Φ should be proportional to $1 - r$. This seems to be the case experimentally for $r \in [0.85; 1]$ despite strong uncertainties in the PIV measurements near the boundary. For r close to 1, the volume $V_p \approx 2\pi(1 - r)h$ is proportional to $1 - r$ and much smaller than V_b such that $T \approx V_p/\Phi$ is in fact independent of r. However, for r smaller than 0.85, the velocity is smaller than its linear variation in $1 - r$. This would lead to an overestimation of the flux Φ in the theory which could explain why the homogenization time T is smaller than in the experiment.

5. Mixing in the presence of vortex breakdown

5.1. Homogenization time

Figure 11 shows the evolution of the dye in the presence of vortex breakdown. The images are completely different from the case without breakdown because the dye is trapped inside the bubble. This creates a sharp interface between the bubble with a strong concentration and the rest of the flow with a weak and homogeneous dye concentration. This clearly shows that the streamline which delimits the bubble is a barrier for transport since it prevents any advection across the streamline in the axisymmetric case.

As a consequence, the dye takes a very long time to escape the bubble, as shown in figure 11. Indeed, even at $t = 4000$ (Fig. 11d), the dye is still concentrated within the bubble although it would be completely homogeneous without vortex breakdown at this tilt angle (see Fig. 8d). It is curious to see that the dye is able to enter the bubble during the injection stage probably because the dye is extremely concentrated at the hyperbolic point. This allows for a sufficient flux of dye toward the bubble (due to the weak non-axisymmetric perturbations) before the dye is spread in the bulk of the cylinder. The images are totally different if the dye is injected outside of the bubble (with a black bubble surrounded by a weak uniform dye) although it leads to the same homogenization time.

Figure 12 shows that the variance decays exponentially but with a characteristic time much larger than in the absence of vortex breakdown. This is clearly shown in Fig. 13(a) where the homogenization time T suddenly jumps by a factor 3 at the onset of vortex
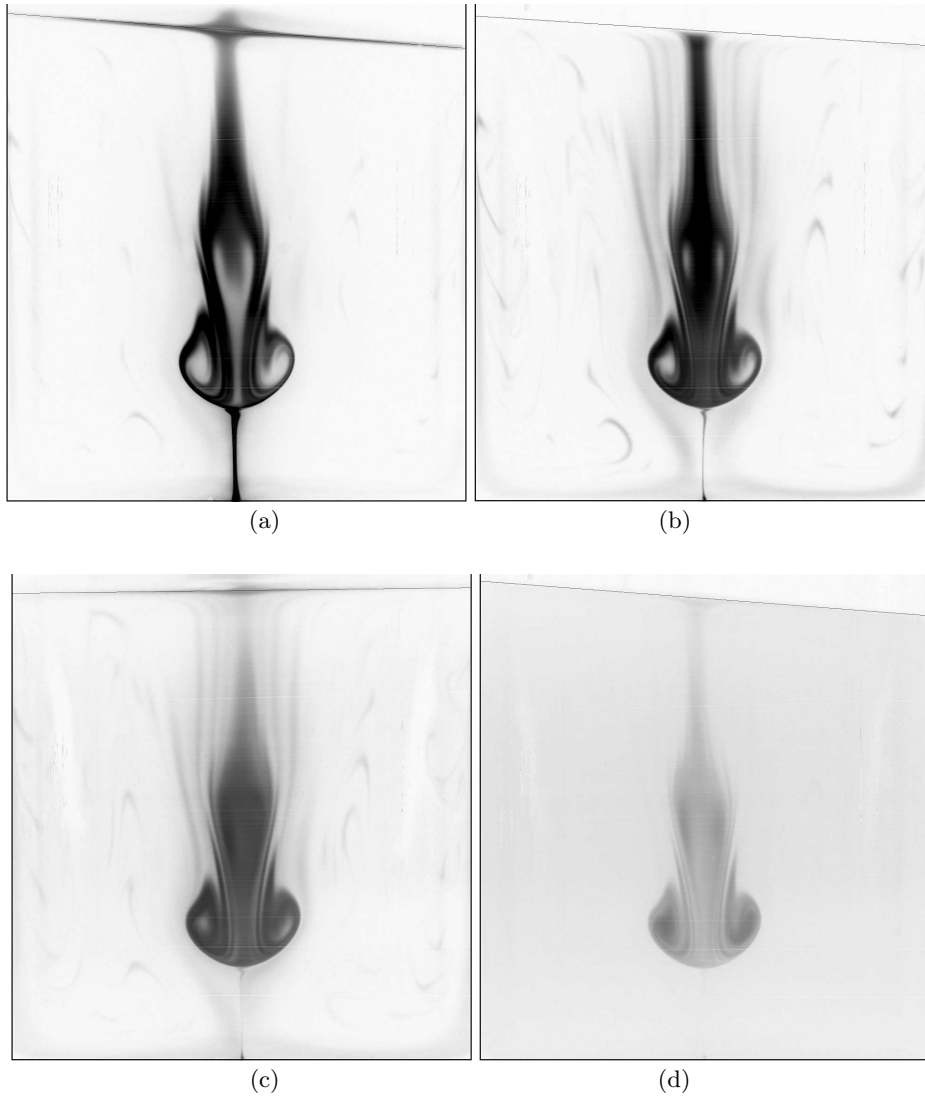
FIGURE 11. Dye visualisation at (a) $t = 0$, (b) $t = 300$, (c) $t = 1000$ and (d) $t = 4000$. $Re = 1900$, $\alpha = 5°$.(negative image of the green component)

breakdown ($Re_c = 1450$). It is curious to see that the homogenization time then decreases with the Reynolds number although the size of the bubble increases. It seems that the homogenization time diverges for small bubbles. At $Re = 2500$, the homogenization time has reached its value without vortex breakdown. It then seems to increase from $Re = 2500$ up to $Re = 3000$, but the data are somewhat noisy and should be interpreted carefully.

Figure 13(b) shows the dependence of the homogenization time T with the tilt angle α of the rotating lid. It is curious to see that it only decreases by 30% (from 3000 to 2000) when the tilt angle α increases by a factor almost 10 (from 2 degrees to 15 degrees). Moreover, the data are quite noisy, as if the mixing was governed by some imperfections of the experiment rather than the tilt angle α. Finally, it can be noted by comparing Figs. 11(a,b) that the asymmetry of the vortex breakdown bubble is stationary and that it does not rotate with the rotating lid. It is thus possible that the asymmetries of the
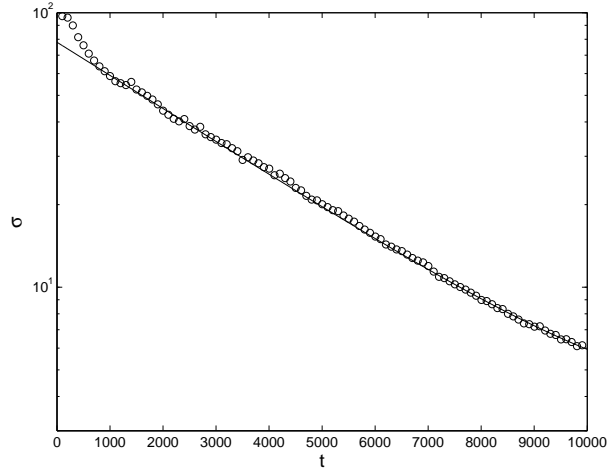
FIGURE 12. Temporal variation of the variance of the image intensity σ in the presence of vortex breakdown ($Re = 1900$). The solid line corresponds to the fit (4.2). $\alpha = 5°$.
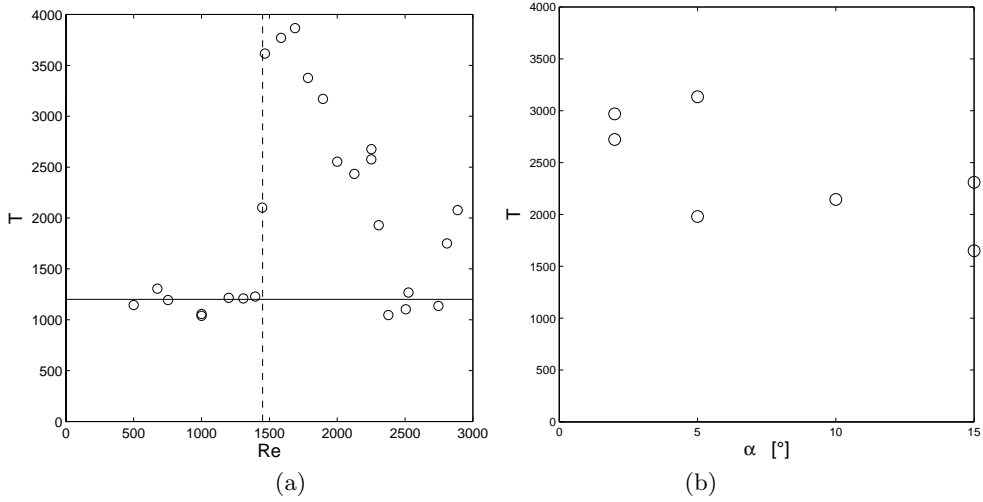

FIGURE 13. Decaying time (a) as a function of the Reynolds number at $\alpha = 5°$ and (b) as a function of the tilt angle α for $Re = 1900$.

bubble are due to a weak angle β of the stationary lid, which is well known to create large disturbances rather than the imposed tilt α of the rotating disk. In order to check this assumption, the tilt angle β has been varied by ± 2.6 degrees with a constant tilt angle α of 5 degrees. Figure 14 shows the structure of the bubble for these two angles. It is clear that the asymmetry of the flow is governed by the tilt angle β and not by the tilt angle α because the two images are symmetric to each other rather than identical. Furthermore, Fig. 15 shows a large variation of the homogenization time T by a factor 10 when the tilt angle β is varied by only 2°. It seems to be correctly fitted to by

$$T = \frac{1600}{\beta - \beta_0}, \tag{5.1}$$

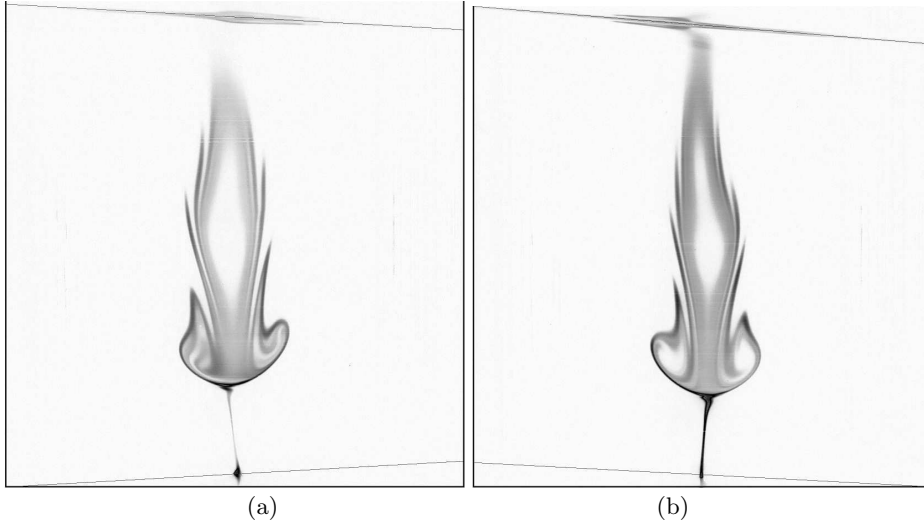where β is given in degrees and $\beta_0 = -0.3°$ is a small angle due to the imperfections

FIGURE 14. Dye visualisation at $t = 0$ for (a) $\beta = 2.6°$ and (b) $\beta = -2.6°$. $Re = 1900$, $\alpha = 5°$.
(negative image of the green component)

of the experimental set-up. An accurate measurement of the shape of the cylinder (from the images) indeed shows that there is probably a small angle of the order of 0.2 ± 0.1 degree. It is surprising to see that a small tilt angle β of the stationary lid (of the order of 1 degree) has more influence on the homogenization time T than a larger tilt angle α of the rotating lid (of the order of 10 degrees). This result is in agreement with the numerical study of Brons *et al.* (2007) who showed that the residence time inside the bubble is extremely sensitive to the tilt angle β. They explained this sensitivity by a decorrelation between the unstable manifold of the lower hyperbolic point P and the stable manifold of the higher hyperbolic point Q. This creates some undulations of these manifolds, responsible for the tongues visible in the visualizations of Fig. 14, as described by Lopez & Perry (1992). In the following, we will try to quantify these tongues and the mixing they generate using the Melnikov theory in this 3D stationary flow, as was done by Rom-Kedar *et al.* (1990) in a 2D flow with a periodic perturbation.

5.2. *Melnikov theory on a model flow*

We first need to model the flow as an axisymmetric bubble $\boldsymbol{u}^0$ together with a perturbation flow $\beta\boldsymbol{u}^1$ proportional to the tilt angle. The axisymmetric flow, presented in Fig. 16, exhibits a bubble located between two hyperbolic (and heteroclinic) points P and Q on the axis, separated by $2\rho \simeq 0.36$ at this Reynolds number (ρ being the radius of the bubble). The angular velocity u_θ/r varies between 0.1 and 0.2 between the lower part and the upper part of the bubble. However, this variation is smaller when the size of the bubble decreases because viscous effects tend to smooth the vorticity. As a consequence, the axisymmetric flow is modeled by the simplest normal form which presents two hyperbolic points P and Q around z_0 and has a constant angular velocity ω. It can be written in cylindrical coordinates as:

$$\mathbf{u}^0 = \left[-\lambda r(z - z_0), \omega r, \lambda((z - z_0)^2 - \rho^2) + \xi r^2 \right]. \tag{5.2}$$

In the following, z_0 will be taken equal to 0 which corresponds to changing the origin of the z-axis. Close to the critical Reynolds number, λ, ξ and ω are constant but ρ vanishes
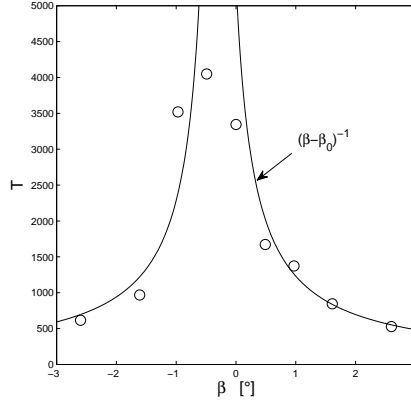
FIGURE 15. Decaying time as a function of the tilt angle β of the bottom stationary disk for $Re = 1900$. $\alpha = 5°$.
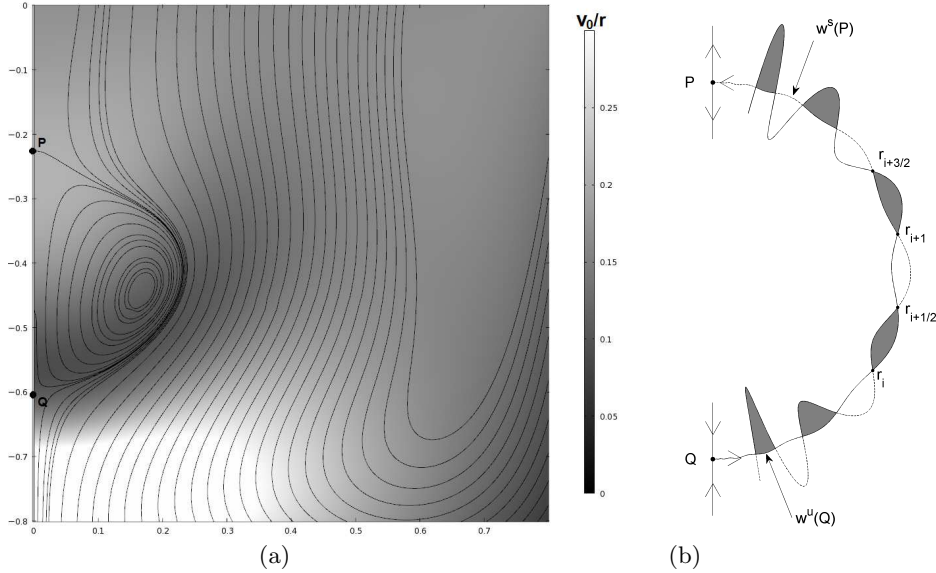

FIGURE 16. (a) Axisymmetric flow $\mathbf{u^0}$ obtained numerically at $\beta = 0$. Solid lines correspond to streamlines and greyscale to the angular velocity u_θ^0/r. (b) Sketch of the stable manifold of P and the unstable manifold of Q in the presence of a periodic perturbation superimposed on the bubble flow $\mathbf{u}^0$. $Re = 1900$

and it should be Taylor expanded to first order, leading to

$$\rho^2 = \zeta(Re - Re_c).$$

The constants are measured using the numerical simulations at $Re = 1900$, which gives $\lambda = 0.25$, $\xi = 0.17$, $\omega = 0.15$ and $\rho = 0.18$ (i.e., $\zeta = 7.2 \times 10^{-5}$). It is well known (Brons *et al.* 2007) that a small non-axisymmetric perturbation creates a difference between the unstable manifold $w^u(Q)$ (i.e. all the points coming from Q at $t = -\infty$) and the stable manifold $w^s(P)$ (i.e., all the points ending in P at $t = +\infty$) In the frame of reference rotating with the bubble at ω, the trajectories remain in a meridional plane, such that the problem reduces to a 2D flow with a periodic perturbation (due to the non axisymmetric
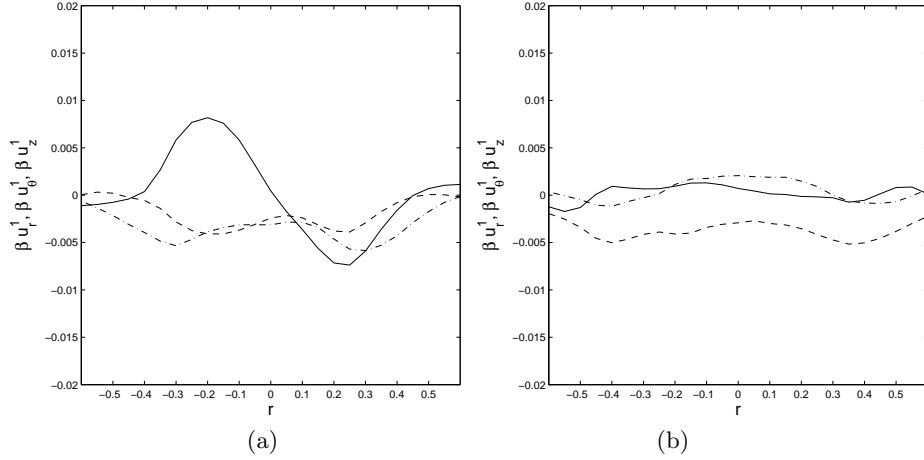
FIGURE 17. Numerical profile of the perturbation velocity $\mathbf{u}^1 = \mathbf{u} - \mathbf{u}^0$ as a function of r along a line oriented at $\theta = -45°$ (a) and $\theta = +45°$ (b) at $z = -0.5$ and $\beta = 2°$. Dashed lines correspond to u_r, dash-dotted lines to u_θ and solid lines to u_z. $Re = 1900$

perturbation rotating at $-\omega$). If these manifolds intersect in a point $\mathbf{r}_i$, they will intersect an infinite number of times, because a period $2\pi/\omega$ later, $\mathbf{r}_i$ is advected in $\mathbf{r}_{i+1}$, which thus belongs to both manifolds $w^u(Q)$ and $w^s(P)$ (see Fig.16b). As shown in Fig. 16(b), this leads to an infinite number of intersection points which delimits lobes between the two manifolds. Moreover, the grey lobe located between $\mathbf{r}_i$ and $\mathbf{r}_{i+1/2}$ and delimited by the two manifolds is advected a period $2\pi/\omega$ later into the next grey lobe between $\mathbf{r}_{i+1}$ and $\mathbf{r}_{i+3/2}$. Finally, as noted by Rom-Kedar *et al.* (1990), the lobes come from the inside of the bubble (i.e., above $w^u(Q)$ at Q) at $t = -\infty$ and are advected outside of the bubble (i.e. above $w^s(P)$ at P) at $t = +\infty$. As a consequence, the volume of this lobe corresponds exactly to the quantity of dye that exits the bubble during one period. The goal of the calculation presented in the following is thus to calculate the volume of this lobe as a function of the non-axisymmetric perturbation.

The perturbation $\beta\mathbf{u}^1$ due to the tilt angle has been evaluated numerically by subtracting the velocity $\mathbf{u}^0$ obtained in a simulation at $\beta = 0$ from the velocity $\mathbf{u}$ obtained in a simulation at $\beta = 2°$. However, since these calculations are three-dimensional and since the perturbation is small (because it is proportional to the small tilt angle β) there is significant noise in the data. The radial profiles of velocity are plotted in Fig. 17 at $\theta = \pm45°$. The main effect of the tilt β is to create a non axisymmetric perturbation in the axial velocity w (solid line), related to a positive (resp. negative) jet at $\theta = -45°$ (resp. $\theta = 135°$). This can be modeled locally as a shear oriented at θ^1, which leads to the velocity field for the perturbation:

$$\mathbf{u}^1 = \left(0, 0, \gamma r \cos(\theta - \theta^1)\right), \qquad (5.3)$$

with $\theta^1 = 135°$ and $\gamma = 0.02$ if β is given in degrees.

The Melnikov theory is applied in the appendix in order to calculate the distance between the stable and the unstable manifolds $w^u(Q)$ and $w^s(P)$. For this purpose, the problem is solved in the frame of reference rotating with the fluid at ω such that the trajectories become two-dimensional. Moreover, we apply a change of variables from (r, z) into $(s = \pi r^2, z)$ so that the 2D flow becomes Hamiltonian. The volume of the lobes is

then easily evaluated such that the homogenization time can be written analytically:

$$T = \frac{\sqrt{2}\rho^3(\lambda\xi)^{3/2}\cosh(\pi\omega/2\lambda\rho)}{\beta\gamma\omega(\lambda^2\rho^2+\omega^2)}. \tag{5.4}$$

The first consequence is that this homogenization time is indeed inversely proportional to the tilt angle β. This simply comes from the fact that the size of the lobes is proportional to β since the Melnikov theory is obtained to first order. The second consequence (less trivial) is that the homogenization time scales as $T \sim \rho^3 \cosh(\pi\omega/2\rho\lambda)$, i.e., a function of ρ, and it thus diverges when the size of the bubble vanishes. This is exactly what has been observed experimentally since T diverges when the Reynolds number gets close to the critical Reynolds number Re_c. Of course, there is a saturation of T due to the molecular diffusion when the size of ρ is of the order of the diffusion length $\sqrt{T/ReS}$, which leads to a diffusive time

$$T = \rho^2 ReSc \simeq 200(Re - Re_c).$$

This explains the rapid increase of the homogenization time at the onset of the vortex breakdown. Finally, it explains why the perturbation due to the tilt angle α of the rotating lid is less efficient than the angle β of the stationary lid. Indeed, the tilted rotating lid creates a non-axisymmetric perturbation which rotates at an angular frequency equal to 1 compared to the laboratory, i.e., at an angular velocity $1 - \omega$ in the frame of reference rotating with the bubble (at ω). In formula (5.4), ω should thus be replaced by $1-\omega$ when looking at the perturbation due to α. Since $\omega = 0.1$, this creates a term $\cosh[\pi(1-\omega)/2\lambda\rho]$ which is extremely large (10^{12} times larger than for the tilt β). This explains why a large tilt $\alpha = 15°$ of the rotating lid has almost no influence on the mixing across the bubble although a small tilt $\beta = 1°$ of the stationary lid has a large impact.

However, despite this qualitative agreement, the quantitative agreement is poor because the numerical values lead to $T = 250/\beta$ at $Re = 1900$ (when β is in degrees), which is 6 times smaller than the experimental result. This could be due to the fact that the concentration within the exiting lobe is not exactly equal to the concentration within the bubble. Indeed, it contains some fluid coming from an incoming lobe at earlier time. This entanglement is known to create a fractal structure in the absence of molecular diffusion (see Rom-Kedar *et al.* 1990; Sotiropoulos *et al.* 2001). This has not been observed here because the Schmidt number is not large enough. However, this effect leads to a weaker escape rate of the scalar which could explain the discrepancy between the experiment and the theory.

6. Conclusion

In this paper, we have presented an experimental and theoretical study on the mixing properties of a helical flow in a motionless cylinder with a rotating end. It was found that the axisymmetric flow is very inefficient for mixing such that any small asymmetry completely governs the homogenization of the dye inside the cylinder. Indeed, the homogenization time is always 2 orders of magnitude smaller than the theoretical diffusive time R^2/κ, because small imperfections of the experimental set-up (here a small tilt of the bottom) create a convective mixing much larger than the diffusive mixing. In order to quantify the influence of the symmetry breaking on the mixing properties, the top ends have been tilted with controlled angles and the homogenization time has been measured accurately as the decaying time of the variance.

The mechanism for mixing strongly depends on the structure of the flow which is well known to exhibit a vortex breakdown bubble for a finite range of Reynolds numbers. In the absence of vortex breakdown, the tilt of the rotating disk induces some inward radial jets at the periphery of the cylinder, which are advected by the mean recirculation inside the bulk of the cylinder. As a consequence, the homogenization time is 3 orders of magnitude smaller than the axisymmetric diffusive time for a small tilt of only 10 degrees. The homogenization time is inversely proportional to the tilt angle and independent of the Reynolds number. These scalings can be explained by a simple model taking into account the flux of scalar between the periphery and the bulk of the cylinder.

In the presence of vortex breakdown, the scalar is trapped within the bubble such that the homogenization time is completely governed by the escape rate from the bubble. Curiously, the tilt of the rotating lid has a weak impact on the mixing. However, the tilt of the stationary lid has a very large influence. The homogenization time is inversely proportional to the tilt angle and seems to diverge when the size of the bubble vanishes. This surprising result can be predicted by using the Melnikov theory to calculate the volume of the lobes which exit from the bubble. As far as we know, this is the first comparison between an experiment and a theoretical derivation of a mixing rate using the Melnikov function.

It should be noted that this Melnikov theory has been usually applied for a 2D flow with a periodic perturbation. It is generalised here for a 3D axisymmetric stationary flow with a non axisymmetric perturbation. However, the angular velocity has to be assumed constant on the whole stable/unstable manifold in order to restrict the problem to a 2D flow in the rotating frame of reference. The result is thus only asymptotically valid for small bubble sizes (i.e., at the onset of vortex breakdown). The full solution could be calculated since the Melnikov theory has been extended to n dimensions by Gruendler (1985) and applied to a vortex breakdown flow by Holmes (1984). However, their calculation is more difficult because the homogeneous problem $\dot{\xi} = Du_0(t)\xi$ has to be solved at any time.

Moreover, although this type of dynamics of a perturbation added to heteroclinic points has been extensively studied in the absence of diffusion, there has never been any result characterizing the effect of the diffusion. However, this effect might largely influence the mixing properties. For example, it was shown here that the fractal properties of the entangled lobes is not recovered because the diffusion is too large. It would be interesting to quantify the cut-off at small scale due to diffusion as a function of the Schmidt number. Diffusion might also smooth the devil's staircase which is obtained in the number of particles trapped in the bubble. It might even change the escape rate of the scalar. Indeed, for small diffusion, the time for the scalar to exit the bubble is probably governed by the diffusion outside of a KAM torus rather than outside of the bubble

since the separatrix is indeed permeable due to the perturbation. In fact, it is clear that there is a gap between the theories developed for homogeneous turbulence with molecular diffusion but without flow structures and the theories developed for dynamical systems with inhomogeneous flow structures but with no diffusion. This paper is an attempt to reconcile the two domains. However, new models still need to be developed in order to predict properly the mixing properties of flows with heterogeneous structures.

Acknowledgements

Appendix

The purpose is to evaluate the volume V_l of the lobes between the unstable and the stable manifolds of the hyperbolic points P and Q in the flow $\mathbf{u^0} + \beta\mathbf{u^1}$ given by (5.2) and (5.3). First, we need to study the problem in the frame of reference rotating at ω such that the trajectories remain in a meridional plane, leading to a 2D problem with a periodic perturbation $u_z^1 = \gamma r \cos(\omega t)$. Second, we make a change of variable because the Melnikov theory can only be applied for a flow which is Hamiltonian to first order. We thus use the surface $s = \pi r^2$ instead of the radial coordinate. Using the relation $ds = 2\pi r dr$, the trajectories $(s(t), z(t))$ are solution of the flow:

$$\begin{pmatrix} \frac{ds}{dt} \\ \frac{dz}{dt} \end{pmatrix} = \begin{pmatrix} u_s^0 \\ u_z^0 \end{pmatrix} + \beta \begin{pmatrix} u_s^1 \\ u_z^1 \end{pmatrix} = \begin{pmatrix} -2\lambda sz \\ \lambda(z^2 - \rho^2) + \xi\frac{s}{\pi} \end{pmatrix} + \beta \begin{pmatrix} 0 \\ \gamma\sqrt{\frac{s}{\pi}}\cos(\omega t) \end{pmatrix} \quad (6.1)$$

To first order, this flow is Hamiltonian because

$$\frac{\partial u_s^0}{\partial s} + \frac{\partial u_z^0}{\partial z} = \frac{\partial(ru_r^0)}{r\partial r} + \frac{\partial u_z^0}{\partial z} = 0.$$

The Hamiltonian (which is called the streamfunction in fluid mechanics) defined by $u_s = -\partial H/\partial z$ and $u_z = \partial H/\partial s$ is equal to

$$H(s, z) = \lambda s(z^2 - \rho^2) + \frac{\xi s^2}{2\pi}.$$

The Hamiltonian is equal to zero on the streamline joining the two hyperbolic points P and Q, such that $s = -2\pi\lambda(z^2 - \rho^2)/\xi$. Introducing this relation in the flow to first order leads to the differential equation $\dot{z} = \lambda(\rho^2 - z^2)$, which is easily integrated, giving the trajectories to first order:

$$s^0(t) = \frac{2\lambda}{\xi}\frac{\pi\rho^2}{\cosh(\lambda\rho t)}, \quad (6.2)$$

$$z^0(t) = \rho\tanh(\lambda\rho t). \quad (6.3)$$

The Melnikov function $M(t_c)$ can now be calculated and corresponds to the distance $D(t_c)$ between the stable manifold of P and the unstable manifold of Q, multiplied by the norm of the velocity (u_s^0, u_z^0). This function is evaluated at $t = 0$ and at the point $(s^0(t_c), z^0(t_c))$ where t_c can be varied from $-\infty$ to $+\infty$. The Melnikov theory (see Guckenheimer & Holmes 1983, for a demonstration) can be applied by following the

trajectory $(s^0(t - t_c), z^0(t - t_c))$ to first order and leads to the simple result that it is equal to:

$$M(t_c) = \beta \int_{-\infty}^{+\infty} \mathbf{u^0}[s^0(t - t_c), z^0(t - t_c)] \times \mathbf{u^1}[s^0(t - t_c), z^0(t - t_c), t] dt. \qquad (6.4)$$

where the cross product $\mathbf{u^0} \times \mathbf{u^1}$ is equal to $u_s^0 u_z^1 - u_z^0 u_s^1$. In our case, this formula is simply written (using a change of variable $\tau = t - t_c$):

$$M(t_c) = -\beta \int_{\tau=-\infty}^{\tau=+\infty} 2\lambda s_0(\tau) z_0(\tau) \gamma \sqrt{\frac{s_0(\tau)}{\pi}} \cos[\omega(\tau + t_c)] d\tau. \qquad (6.5)$$

This integral can be evaluated by splitting the cosine function and using the residue theorem, which leads to

$$M(t_c) = \frac{2\sqrt{2}\beta\gamma\pi^2\omega(\lambda\rho^2 + \omega^2)\sin(\omega t_c)}{3(\lambda\xi)^{3/2}\cosh(\pi\omega/2\rho\lambda)}. \qquad (6.6)$$

As noted by Rom-Kedar *et al.* (1990), this function completely governs the transport across the streamline because the volume of the lobes is equal to

$$V_L = \int_{r_i}^{r_{i+1/2}} D(t_c) dl = \int_{t_i}^{t_{i+1/2}} M(t_c) dt_c \qquad (6.7)$$

since $dl = \|u_0\| dt$. Here t_i, $t_{i+1/2}$ are two consecutive times at which the manifolds intersect (i.e., where $M(t_0) = 0$); for example $t_i = 0$ and $t_{i+1/2} = \pi/\omega$. It should be noted that this result was derived in 2D by Rom-Kedar *et al.* (1990); however, it can be used in 3D here because the volume element $2\pi r dr dz$ is equal to the surface element $ds dz$ by definition of s. The volume of each lobe is thus equal to:

$$V_L = \frac{4\sqrt{2}\beta\gamma\pi^2(\lambda\rho^2 + \omega^2)}{3(\lambda\xi)^{3/2}\cosh(\pi\omega/2\lambda\rho)}. \qquad (6.8)$$

Finally, after each rotation period $2\pi/\omega$, each lobe has been translated from r_i to r_{i+1}, such that the rate of scalar c which exits the bubble is equal to $cV_L\omega/2\pi$. Since the volume of the bubble is approximately equal to $V_B = 4\pi\rho^3/3$, the conservation of the scalar leads to $V_B dc/dt = V_L\omega/2\pi$ such that the scalar c decreases exponentially with a decaying time equal to:

$$T = \frac{2\pi V_B}{\omega V_L} = \frac{\sqrt{2}\rho^3(\lambda\xi)^{3/2}\cosh(\pi\omega/2\lambda\rho)}{\beta\gamma\omega(\lambda^2\rho^2 + \omega^2)}. \qquad (6.9)$$

REFERENCES

ANTONSEN, T. M., FAN, Z., OTT, E. & GARCIA-LOPEZ, E. 1996 The role of chaotic orbits in the determination of power spectra of passive scalars. *Phys. Fluids* **8** (11), 3094–3104.

BATCHELOR, G. K. 1959 Small-scale variation of convected quantities like temperature in a turbulent fluid. Part 1. General discussion and the case of small conductivity. *J. Fluid Mech.* **5**, 113–133.

BENJAMIN, T. B. 1962 Theory of the vortex breakdown phenomenon. *J. Fluid Mech* **14**, 593–629.

BRONS, M., SHEN, W. Z., SORENSEN, J. N. & ZHU, W. J. 2007 The influence of imperfections on the flow structure of steady vortex breakdown bubbles. *J. Fluid Mech.* **578**, 453–466.

BRONS, M., THOMPSON, M. & HOURIGAN, K. 2009 Dye visualization near a three-dimensional stagnation point: application to the vortex breakdown bubble. *J. Fluid Mech.* **622**, 177–194.

BURGGRAF, O. R. & FOSTER, M. R. 1977 Continuation or breakdown in tornado like vortices. *J. Fluid Mech* **80**, 685.

DUPLAT, J. & VILLERMAUX, E. 2008 Mixing by random stirring in confined mixtures. *J. Fluid Mech.* **617**, 51–86.

DUSTING, J., SHERIDAN, J. & HOURIGAN, K. 2006 A fluid dynamics approach to bioreactor design for cell and tissue culture. *Biotechnology and Bioengineering* **94**, 1196–1208.

ESCUDIER, M. P. 1984 Observations of the flow produced in a cylindrical container by a rotating endwall. *Experiments in Fluids* **2**, 189–196.

ESCUDIER, M. P. 1988 Vortex breakdown: Observations and explanations. *Prog. Aerop. Sci.* **25**, 189.

FALER, J. H. & LEIBOVICH, S. 1978 An experimental map of the internal structure of a vortex breakdown. *J. Fluid Mech* **86**, 313–335.

FOUNTAIN, G. O., KHAKAR, D. V. & OTTINO, J. M. 1998 Visualization of three-dimensional chaos. *J. Fluid Mech* **281**, 683–686.

GALLAIRE, F., RUITH, M., MEIBURG, E. & CHOMAZ, J. M. 2006 Spiral vortex breakdown as a global mode. *J. Fluid Mech* **549**, 71–80.

GELFGAT, A. Y., BAR-YOSEPH, P. Z. & SOLAN, A. 1996 Stability of confined swirling flow with and without vortex breakdown. *J. Fluid Mech* **311**, 1–36.

GELFGAT, A. Y., BAR-YOSEPH, P. Z. & SOLAN, A. 2001 Three-dimensional instability of axisymmetric flow in a rotating lid-cylinder enclosure. *J. Fluid Mech* **438**, 363–377.

GOUILLART, E., KUNCIO, N., DAUCHOT, O., DUBRULLE, B., ROUX, S. & THIFFEAULT, J.-L. 2007 Walls inhibit chaotic mixing. *Phys. Rev. Lett.* **99**, 114501.

GRUENDLER, J. 1985 The existence of homoclinic orbits and the method of melnikov for systems in *rn*. *SIAM J. Math. Anal.* **16** (5), 907–931.

GUCKENHEIMER, J. & HOLMES, P. 1983 *Non-Linear Oscillations, Dynamical Systems and Bifurcations of Vector Fields*. Springer.

GUPTA, A. K., LILLEY, D. G. & SYRED, N. 1984 *Swirl flows*. Abacus, Kent, England.

HALL, M. G. 1972 Vortex breakdown. *Ann. Rev. Fluid Mech* **4**, 195–218.

HARVEY, J. K. 1962 Some observations of the vortex breakdown phenomenon. *J. Fluid Mech* **14**, 585.

HAYNES, P. H. & VANNESTE, J. 2005 What controls the decay of passive scalars in smooth flows? *Phys. Fluids* **17**, 097103.

HINDMARSH, A. C., BROWN, P. N., GRANT, K. E., LEE, S. L., SERBAN, R., SCHUMAKER, D. E. & WOODWARD, C. S. 2005 Suite of nonlinear and differential/algebraic equations solvers. *ACM Transactions on Mathematical Software (TOMS)* **31** (3), 363–396.

HOLMES, P. 1984 Contemp. math. *Physics of Fluids* **28**, 393–403.

ISMADI, M. P., MEUNIER, P., FOURAS, A. & HOURIGAN, K. 2011 Experimental control of vortex breakdown by density effects. *Physics of Fluids* **23**, 034104.

KALDA, J. 2000 Simple model of intermittent passive scalar turbulence. *Phys. Rev. Lett.* **84** (3), 471–474.

LEIBOVICH, S. 1978 The structure of vortex breakdown. *Ann. Rev. Fluid Mech* **10**, 221–246.

LOPEZ, J. M. 2006 Rotating and modulated rotating waves in transitions of an enclosed swirling flow. *J. Fluid Mech* **553**, 323–346.

LOPEZ, J. M. 2012 Three-dimensional swirling flows in a tall cylinder driven by a rotating endwall. *Phys. Fluids* **24**, 014101.

LOPEZ, J. M. & PERRY, A. D. 1992 Axisymmetric vortex breakdown. part 3 onset of periodic flow and chaotic advection. *J. Fluid Mech* **234**, 449–471.

LOWSON, M. V. & RILEY, A. J. 1995 Vortex breakdown control by delta wing geometry. *J. Aircraft* **32** (4), 832–838.

MELIGA, P., GALLAIRE, F. & CHOMAZ, J. M. 2012 A weakly nonlinear mechanism for mode selection in swirling jets. *J. Fluid Mech* **699**, 216–262.

MEUNIER, P. & LEWEKE, T. 2003 Analysis and optimization of the error caused by high velocity gradients in PIV. *Exp. Fluids* **35**, 408–421.

MEUNIER, P. & VILLERMAUX, E. 2010 The diffusive strip method for scalar mixing in two dimensions. *J. Fluid Mech* **662**, 134–172.

PIERREHUMBERT, R. T. 1994 Tacer structure in the large-eddy dominated regime. *Chaos Solitons Fractals* **4**, 1111–1116.

ROM-KEDAR, V., LEONARD, A. & WIGGINS, S. 1990 An analytical study of transport, mixing and chaos in an unsteady vortical flow. *J. Fluid Mech* **214**, 347–394.

RONNENBERG, B. 1977 Ein selbstjustierendes 3-komponenten-LDA nach dem Vergleighstrahlverfaren, angewendt für Untersuchungen in einer stationaren zylindersymmetrischen Drehströmung mit einem Rühckströmgebiet. *Technical Report Bericht 20, Max-Planck-Institut für Strömungsforschung, Göttingen* .

ROTUNNO, R. 2012 The fluid dynamics of tornadoes. *Annu. Rev. Fluid Mech* **45**, 59–84.

RUITH, M. R., CHEN, P., MEIBURG, E. & MAXWORTHY, T. 2003 Three-dimensional vortex breakdown in swirling jets and wakes: direct numerical simulation. *J. Fluid Mech* **486**, 331–378.

SARPKAYA, T. 1971 On stationary and travelling vortex breakdowns. *J. Fluid Mech* **45**, 545–559.

SORENSEN, J. N., NAUMOV, I. V. & OKULOV, V. L. 2011 Multiple helical modes of vortex breakdown. *J. Fluid Mech* **683**, 430–441.

SOTIROPOULOS, F., VENTIKOS, Y. & LACKEY, T. C. 2001 Chaotic advection in three-dimensional stationary vortex-breakdown bubbles: Sil'nikov's chaos and the devil's staircase. *J. Fluid Mech* **444**, 257–297.

SOTIROPOULOS, F., WEBSTER, D. R. & LACKEY, T. C. 2002 Experiments on lagrangian transport in steady vortex-breakdown bubbles in a confined swirling flow. *J. Fluid Mech* **466**, 215–248.

SPOHN, A., MORY, M. & HOPFINGER, E. J. 1998 Experiments on vortex breakdown in a confined flow generated by a rotating disc. *J. Fluid Mech* **370**, 73–99.

THIFFEAULT, J. L., DOERING, C. R. & GIBBON, J. D. 2004 A bound on mixing efficiency for the advection diffusion equation. *J. Fluid Mech.* **521**, 105–114.

THOMPSON, M. C. & HOURIGAN, K. 2003 The sensitivity of steady vortex breakdown bubbles in confined cylinder flows to rotating lid misalignment. *J. Fluid Mech.* **496**, 129138.

THOUAS, G. A., SHERIDAN, J. & HOURIGAN, K. 2007 A bioreactor model of mouse tumor progression. *J. Biomedicine Biotechnology* **9**, 32754.

TOUSSAINT, V., CARRIÈRE, P. & RAYNAL, F. 1995 A numerical Eulerian approach to mixing by chaotic advection. *Phys. Fluids* **7**, 2587–2600.

TOUSSAINT, V., CARRIÈRE, P., SCOTT, J. & GENCE, J. N. 2000 Spectral decay of a passive scalar in chaotic mixing. *Phys. Fluids* **12** (11), 2834–2844.

VOGEL, H. U. 1968 Experimentelle Ergebnisse über die laminare Strömung in einem zylindrischen Gehaüse mit darin rotierender Scheibe. *Technical Report Bericht 6, Max-Planck-Institut für Strömungsforschung, Göttingen* .

WANG, S. & RUSAK, Z. 1997 The dynamics of a swirling flow in a pipe and transition to axisymmetric vortex breakdown. *J. Fluid Mech.* **340**, 177–223.

WARHAFT, Z. 2000 Passive scalars in turbulent flows. *Annu. Rev. Fluid Mech.* **32**, 203–240.

WENTZ, W. H. & KOHLMAN, D. L. 1971 Vortex breakdown on slender sharp-edged wings. *J. Aircraft* **8** (3), 156–161.

WIGGINS, S. 2003 *Introduction to Applied Nonlinear Dynamical Systems and Chaos*. Springer.